



**HAL**  
open science

## Liquid inertia versus bubble cloud buoyancy in circular plunging jet experiments

Narendra Dev, J. John Soundar Jerome, H el ene Scolan, Jean-Philippe Matas

► **To cite this version:**

Narendra Dev, J. John Soundar Jerome, H el ene Scolan, Jean-Philippe Matas. Liquid inertia versus bubble cloud buoyancy in circular plunging jet experiments. *Journal of Fluid Mechanics*, In press, 978, pp.A23. 10.1017/jfm.2023.1019 . hal-04314923

**HAL Id: hal-04314923**

**<https://hal.science/hal-04314923>**

Submitted on 29 Nov 2023

**HAL** is a multi-disciplinary open access archive for the deposit and dissemination of scientific research documents, whether they are published or not. The documents may come from teaching and research institutions in France or abroad, or from public or private research centers.

L'archive ouverte pluridisciplinaire **HAL**, est destin ee au d ep ot et  a la diffusion de documents scientifiques de niveau recherche, publi es ou non,  emanant des  tablissements d'enseignement et de recherche fran ais ou  trangers, des laboratoires publics ou priv es.

# Liquid inertia versus bubble cloud buoyancy in circular plunging jet experiments

Narendra Dev, J. John Soundar Jerome, H  l  ne Scolan and Jean-Philippe Matas†

Univ Lyon, Univ Claude Bernard Lyon 1, CNRS, Ecole Centrale de Lyon, INSA Lyon, LMFA, UMR5509, 69622 Villeurbanne France

(Received xx; revised xx; accepted xx)

When a liquid jet plunges into a pool, it can generate a bubble-laden jet flow underneath the surface. This common and simple phenomenon is investigated experimentally for circular jets to illustrate and quantify the role played by the net gas/liquid void fraction on the maximum bubble penetration depth. It is first shown that an increase in either the impact diameter or the jet fall height to diameter ratio at constant impact momentum leads to a reduction in the bubble cloud size. By systematically measuring the local void fraction using optical probes in the biphasic jet, it is then demonstrated that this effect is a direct consequence of the increase in the air content within the cloud. A simple momentum balance model, including only inertia and the buoyancy force, is shown to predict the bubble cloud depth without any fitting parameters. Finally, a Froude number based on the bubble terminal velocity, the cloud depth, and also the net void fraction is introduced to propose a simple criterion for the threshold between the inertia-dominated and buoyancy-dominated regimes.

**Key words:**

---

## 1. Introduction

The impact of a plunging jet on the free surface of a pool of the same or different liquid above a critical velocity transports ambient gas into the continuous liquid phase forming a cluster of bubbles, a bubble cloud (Lin & Donnelly 1966; Bonetto *et al.* 1994; Zhu *et al.* 2000; Lorenceau *et al.* 2004). This phenomenon is widely encountered in industrial applications like the stirring of chemicals (McKeogh & Ervine 1981) or hydroelectric applications (Guyot 2019), and in nature, as in breaking waves and cascades (Chanson 2002; Kiger & Duncan 2012).

Previous studies discussed the inception of air bubbles below jet impact, and proposed models for the air entrainment mechanism based on the morphology in circular and (McKeogh & Ervine 1981; Sene 1988; El Hammoumi *et al.* 2002), planar jets (Cummings & Chanson 1999; Bertola *et al.* 2018), and multi-droplet streams (Speirs *et al.* 2018). Kiger & Duncan (2012) reviewed the air-entrainment mechanism for laminar, turbulent and disintegrated jets of different viscosity. Once the bubble entrainment conditions are reached, the maximum penetration depth of the bubble cloud, denoted as  $H$  in figure 1(a), is an essential parameter to model in various applications (Clanet & Lasheras 1997). Indeed a change in  $H$  will affect the volume of the biphasic region and alter the gas mixing rate in chemical industries. In hydroelectric power plants,  $H$  is critical in designing dams to prevent erosion and structural weakening caused by the incoming biphasic jet hitting the riverbed. As can be inferred from Table 1, previous studies have addressed the bubble cloud formation over a wide range of scales (Bi  n 1993; Clanet & Lasheras

† Email address for correspondence: jean-philippe.matas@univ-lyon1.fr

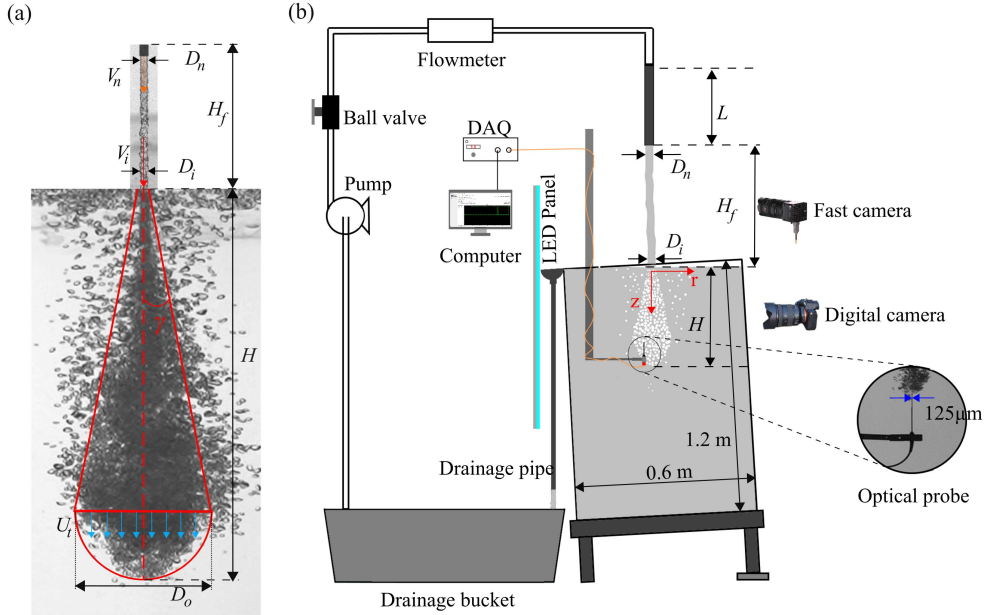


FIGURE 1. (a) Schematic of control volume of the bubble cloud, and (b) Schematic of the experimental setup illustrating flow lines to generate bubble cloud, back-lighting imaging setup and void fraction measurement setup with optical probes.

1997; Chirichella *et al.* 2002; Roy *et al.* 2013; Qu *et al.* 2013; Harby *et al.* 2014; Kramer *et al.* 2016; Miwa *et al.* 2018; Guyot *et al.* 2020). Evidence for strong scale effects exist not only regarding bubble cloud size but also for bubble count rate or void fraction (Chanson *et al.* 2004). Whereas numerous empirical correlations for the cloud depth can be found in the literature depending on their size from a few centimetres to about a few metres, the underlying physics has only been recently elaborated.

In this context, Clanet & Lasheras (1997) developed a jet momentum conservation argument, similar to Suciú & Smigelschi (1976), but by postulating that (i) the biphasic jet expands with a constant cone half-angle  $\gamma = 12.5^\circ$ , as it is well known in turbulent jets (Horn & Thring 1956; Ervine & Falvey 1987; L'vov *et al.* 2008), and (ii) bubbles would escape the biphasic zone as soon as the local advection speed, due to liquid jet below the free-surface, decreases down to the terminal velocity  $U_t$ . They thereby derive a simple prediction for the bubble cloud depth  $H_c$ :

$$H_c = \frac{1}{2 \tan \gamma} \left( \frac{V_i D_i}{U_t} \right), \quad (1.1)$$

where  $V_i$  is the impact velocity and  $D_i$  the impact diameter. Note that there is no adjustable parameter nor any liquid or gas physical properties in equation (1.1), except for  $U_t$  which is taken equal to 22 cm/s for all air bubbles in water larger than 1 mm in diameter (Maxworthy *et al.* 1996). Eq. (1.1) shows that in this case, the cloud depth is directly proportional to  $V_i D_i$ , which, up to a factor of liquid density  $\rho$ , is the square root of the impact momentum. Clanet & Lasheras (1997) obtain a very good agreement for their experiments with micro-jets, of at most 2.16 mm in nozzle diameter. However, unlike single-phase jets in a neutrally-buoyant environment, momentum conservation may not be valid for voluminous biphasic jets, for which buoyancy cannot be neglected. For example, in a 15 cm deep conical bubble cloud which contains only a small void fraction of air, say  $\phi = 10\%$ , the outgoing momentum  $\dot{Q}_o \sim (1 - \phi)\rho U_t^2 \pi H^2 \tan^2 \gamma$  in

Author(s) (year)	Jet and Nozzle geometry	$D_n$ (mm)	$V_n$ (m s <sup>-1</sup> )	$H_f$ (cm)	Re = $\rho V_n D_n / \mu$ (max)
Lin & Donnelly (1966)	↓○	2-8	0.8-2	1-17	$2.5 \times 10^3$
Van de Sande & Smith (1973, 1976)	↙○	2.85-10	3-25	10-40	$1.12 \times 10^5$
van de Donk (1981)	↓○	4-30	4-10	20-85	$2.8 \times 10^5$
McKeogh & Ervine (1981)	↙↓○	6-30	1-7	50-500	$1.1 \times 10^5$
Clanet & Lasheras (1997)	↓○	0.24-2.16	1.9-18	0.7-4	$1.4 \times 10^4$
Cummings & Chanson (1999)	↓□	3 – 10	1.1-2	0.5-18	$1.16 \times 10^4$
Chanson & Manasseh (2003)	↓○	14-25	0.5-5	5-20	$1.6 \times 10^5$
Chanson <i>et al.</i> (2004)	↓○	6.8-25	1.7-4.4	3-10	$1.23 \times 10^5$
Harby <i>et al.</i> (2014)	↓○	4-14	2.5-13	2.5-30	$9 \times 10^4$
Kramer <i>et al.</i> (2016)	↓○	13-81.9	5-7	20-100	$6.4 \times 10^5$
Bertola <i>et al.</i> (2018)	↓□	10.4 – 11.5	2.4-7.4	10.4-12.7	$9.4 \times 10^4$
Guyot <i>et al.</i> (2019)	↔○	0.3-2.4	1.89-20	0.6-4.8	$2.4 \times 10^4$
Guyot <i>et al.</i> (2020)	↓○	0.3-213	3-28	20-950	$3 \times 10^6$
Present study	↓○	2.7-10	2.5-10	5-80	$1 \times 10^5$

TABLE 1. Flow conditions in previous works on vertical (↓), inclined (↙), and oscillating (↔) plunging jets from circular (○) and planar (□) nozzles. All authors used water. Data in Lin & Donnelly (1966) refers also to oil and glycol jets.

Fig. 1(a) is already comparable with the net buoyancy force  $F_b \sim \phi \rho g \pi H^3 \tan^2 \gamma / 3$  acting on it. Indeed, the largest cloud in experiments by Clanet & Lasheras (1997) is about 16 cm deep, and equation (1.1) over-predicts the cloud depth data in the previous literature (Biń 1993, see Fig. 29 and references within) for much deeper clouds.

More recently, Guyot *et al.* (2020) extended the above momentum balance model by accounting for buoyancy effects under the assumption that the void fraction within the bubble cloud was uniform. They applied the momentum balance across the truncated conical control volume in Fig. 1(a) to obtain the following equation for the modelled cloud depth  $H_b$ :

$$\underbrace{\rho V_i V_n \frac{\pi D_n^2}{4}}_{\text{Incoming momentum flux}} = \underbrace{(1 - \bar{\phi}) \rho U_i^2 \pi \left( H_b \tan \gamma + \frac{D_i}{2} \right)^2}_{\text{Outgoing momentum flux}} + \underbrace{\bar{\phi} \rho g \pi \left( \frac{1}{3} H_b^3 \tan^2 \gamma + \frac{D_i}{2} H_b^2 \tan \gamma + \frac{D_i^2}{4} H_b \right)}_{\text{Buoyancy force}}, \quad (1.2)$$

where  $D_n$  is the nozzle diameter,  $V_n$  the velocity at the nozzle, and  $\bar{\phi}$  the constant void fraction. Note that the impact void fraction and diameter have been removed from the impact momentum term on the left-hand side using mass conservation,  $V_n D_n^2 = (1 - \bar{\phi}) V_i D_i^2$ . For the limiting case of micro-jets and bubble cloud depth of 10 cm or lesser, the buoyancy force might become less important compared to the outgoing momentum flux in Eq. (1.2), which then reduces to Eq. (1.1). Conversely, in the limit of very large jets, or massive bubble clouds  $H > 20$  cm, the contribution of the outgoing momentum flux becomes negligible, and Eq. (1.2) reduces to the impact momentum being consumed entirely by buoyancy. The fact that a contribution proportional to a surface-term is balanced by a contribution proportional to a volume-term then leads to  $H$  being proportional to  $(V_i V_n)^{1/3} D_n^{2/3}$ . This is close to the empirical correlation  $H \propto (V_n D_n)^{0.66}$  proposed by van de Donk (1981) and  $H \propto (V_n D_n)^{0.7}$  proposed by McKeogh & Ervine (1981). Hence, based on physical arguments, Eq. (1.2) elucidates the two most common empirical relations,

namely,  $H \propto V_n D_n$  and  $H \propto (V_n D_n)^{0.68}$ , over a very wide range of jet diameters and all available data in the current literature (Biń 1993; Guyot *et al.* 2020).

Furthermore, all parameters in the cubic polynomial for  $H_b$  are known a priori, except for the average gas/liquid void fraction  $\bar{\phi}$ . So, Guyot *et al.* (2020) admitted  $\bar{\phi} = 15\%$  based on results from past studies (McKeogh & Ervine 1981; van de Donk 1981), and obtained a relatively good agreement with large-scale experiments. However, they observed a significant dispersion for the cloud depth both in their data and previous investigations when the jet diameter is large. Guyot *et al.* (2020) attributed this dispersion to the variations in the void fraction  $\bar{\phi}$  between various experiments since it is expected to depend strongly on both the jet geometry and dynamics (McKeogh & Ervine 1981; Sene 1988; Bonetto *et al.* 1994; Zhu *et al.* 2000). Therefore, even if the scaling law for the bubble cloud depth is understood to some extent, measurements of the actual values of the void fraction  $\phi$  are needed to clarify the role of this quantity on the observed dispersion in the cloud depth data. The conditions for the transition from jet momentum-dominated to buoyancy-dominated clouds remain to be established as well. In addition, such investigations can provide insights on how, when and where additional features of the bubble cloud such as turbulent dissipation, bubble size distribution, and bubble cloud shape are necessary for dimensioning industrial applications.

Biń (1993) lists correlations based on both *global* gas/liquid entrainment ratio measurements, using gas-hold up techniques, and *local* gas/liquid void fraction  $\phi$  measurements, often using resistivity probes within a bubble cloud. More recent developments on various correlations, along with inception conditions and some mechanistic viewpoints on air-entrainment rate can be found in Kiger & Duncan (2012). Past studies evidence that in the developing region,  $\phi$  radial profiles consist of two maxima located at the radius of the free jet and a minima at the jet axis (van de Donk 1981; Bonetto & Lahey 1993; Cummings & Chanson 1997; Brattberg & Chanson 1998; Chanson & Manasseh 2003; Ma *et al.* 2010). McKeogh & Ervine (1981) and van de Donk (1981) measured  $\phi$  in the fully-developed region and reported that the peak void fraction  $\phi_0$  occurs along the cloud axis, remains almost constant with depth and then sharply decreases. However, the current literature lacks measurements of cloud depth  $H$  along with measurements of local void fraction  $\phi$  in the developed zone of the plume. Such data over various impact momentum and jet fall-height is necessary to help better understand the dynamics of bubble clouds in the buoyancy-dominated regime.

To address this gap, the objective of the present work is to report concurrent *local* void fraction  $\phi$  and bubble cloud depth  $H$  measurements, for three typical nozzle diameters, and at several impact momentum and fall-heights  $H_f$ . Thereby, our aim is two-fold: we examine not only the robustness and the relevance of the momentum balance models (Suciu & Smigelschi 1976; Clanet & Lasheras 1997; Guyot *et al.* 2020) by incorporating *in-situ* void fraction data into Eqn. (1.2), but also its role on the maximum penetration depth of a two-phase plume, by independently varying three major parameters, namely, nozzle diameter, impact momentum, and fall height. Using such a case study, we also try to propose a simple criterion to determine when the bubble cloud size is controlled by inertia, and when it is controlled by buoyancy.

## 2. Methodology

Lab-scale experiments are carried out using a 1.2 m  $\times$  0.6 m  $\times$  0.6 m glass tank which is slightly tilted on one side so that overflowing water is drained through a drainage pipe to the reservoir bucket to keep the water level constant as shown in Fig. 1(b). Pumps supply water from the drainage bucket to the straight injector, from which it is issued as a plunging jet. Three nozzle diameters  $D_n$  are used:  $D_n = 2.7, 8$  and 10 mm. For nozzle diameter  $D_n = 2.7$  mm, a series of two centrifugal pumps from Pan World (NH-100PX and NH-200PS) is used. A heavy-duty centrifugal pump (2KVC AD 45/80M) from DAB Pumps generates the jet from the larger

8 mm and 10 mm injectors. The injector length-to-diameter ratio ( $L/D_n$ ) is kept equal to 50, and the height of fall-to-diameter ratio  $H_f/D_n$  is varied from 20 up to 100. Nozzle velocity  $V_n$  varies between 1.5 to 12 m/s and is controlled using a flowmeter and ball valve. Impact velocity  $V_i$  is deduced using equation  $V_i = \sqrt{V_n^2 + 2gH_f}$ . The present work only considers the cases where the jet is not broken into droplets before impact.

Backlight imaging is used to film the jet just before the impact illuminated by LED panel using a CMOS fast camera from Ximea (CB262MG) at 300 FPS and 20  $\mu\text{s}$  shutter speed at  $2496 \times 2418$  resolution. Images of the biphasic bubble cloud are filmed using a digital camera (Sony a7 III) and a zoom lens (Sony FE 24-70mm F/4 ZA OSS Carl Zeiss, focal length kept at 35 mm) at 50 FPS and 200  $\mu\text{s}$  exposure at a resolution of  $1920 \times 1080$  pixels. Using a MATLAB-integrated calibration application, lens distortion was found negligible and a constant spatial resolution of 54 and 333  $\mu\text{m}/\text{pixel}$  was used for jet and bubble cloud images, respectively. The cloud images are analysed using the open-source freeware *ImageJ* (Schindelin *et al.* 2012) and algorithms therein for brightness thresholding (Kapur *et al.* 1985; Tsai 1985), along with an *in-house* MATLAB code to detect and trace the outer boundaries of the cloud in order to measure  $H$ . The mean penetration depth,  $H$ , is measured by averaging over 3000 images. A low frame rate was chosen in order to ensure that the images of the bubble cloud are decorrelated and so that the ensemble average value of the cloud depth  $H$  converges faster for a given number of images.

The contours of jet are extracted from images using machine-learning-based object detection models, namely, Grounding DINO (Liu *et al.* 2023) and Segment Anything Model (SAM) (Kirillov *et al.* 2023). The detected jet edges are then analysed using an *in-house* MATLAB code to obtain the impact diameter ( $D_i$ ) and the roughness ( $\epsilon$ ). The latter is defined as the average of the RMS values of the lateral departure from the mean edge position, for each side, and is obtained by averaging over 200 images.

The local void fraction  $\phi$  is measured using an optical fiber probe (A2 Photonics Sensors) of diameter 125  $\mu\text{m}$  mounted upright on a slender plate (thickness = 4 mm), as shown in the magnified view in Fig. 1(b). This horizontal plate is fixed to a vertical cylindrical rod (diameter = 1.5 cm). The probe tip is located at 4.5 cm upstream of this arm. This ensures that obstruction to the incoming flow is minimized as much as possible at the probe tip, where the measurement is carried out. The probe assembly is translated in the vertical plane ( $r$ - $z$  plane) using two motorized linear stages (Igus) having an accuracy of 0.01 mm. The probe signals are sampled at 250 kHz for 60 seconds, a duration which is enough to ensure convergence of the void fraction for all conditions. The signals are analysed using A2 Photonics software (SO6 v4.7). The probe is centered at the jet axis and the measurements are carried out in the radial direction of the cloud with a step size of 2 mm to obtain radial void fraction profiles. This was repeated at various depths such that  $z/H = 0.4, 0.6, \text{ and } 0.8$ . Note that when the bubble cloud size is measured, the probe assembly is pulled out of the tank with the help of the translation stage.

### 3. Results and discussion

#### 3.1. Measurement of bubble cloud depth $H$

Figure 2 illustrates the variation of  $H$  for the  $D_n = 2.7$  mm and  $D_n = 8$  mm nozzles, as a function of  $\sqrt{V_i V_n} D_n$ , which is proportional to the square root of the impact momentum flux, up to a factor  $\rho$ , as in equation (1.2). Note that the largest bubble cloud obtained for our conditions is 45 cm deep, which is significantly smaller than the tank depth (1.25 m). We therefore assume that there is no significant pressure gradient caused by confinement effects in our experiments. The bubble cloud size  $H$  for jets issued from the  $D_n = 2.7$  mm nozzle (red and black discs) varies linearly with  $\sqrt{V_i V_n} D_n$ . This is consistent with the model proposed by Clanet & Lasheras (1997) (solid line), equation (1.1), since for this small-scale jet and for the experimental range considered

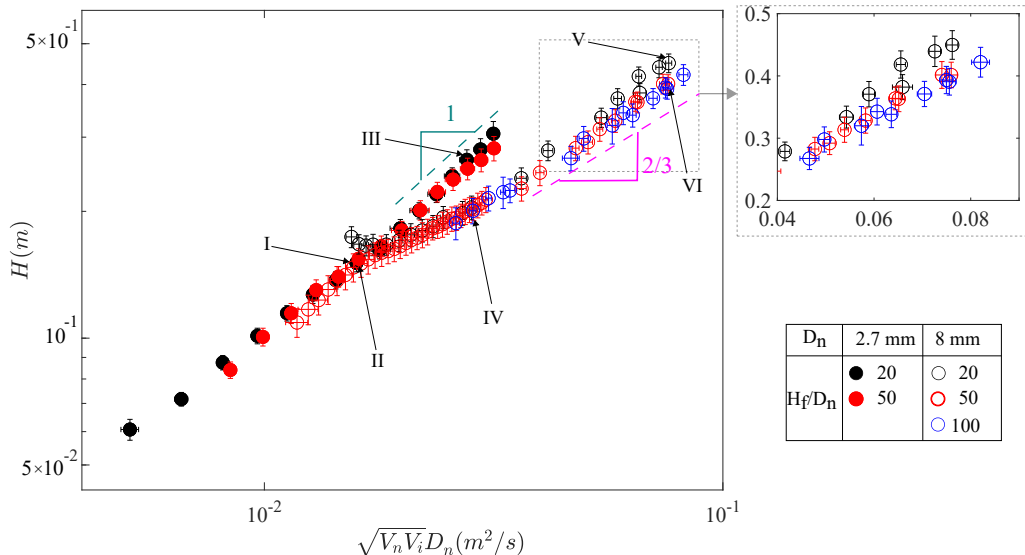


FIGURE 2. Variation of  $H$  with square root of impact momentum  $\sqrt{V_i V_n D_n}$  for  $D_n = 2.7$  and 8 mm at various  $H_f/D_n$ . The solid line shows the trend expected from Eq. (1.1). The dashed line shows the 2/3 scaling law expected at large scales. The inset graph on the top-right is a blow-up of the  $D_n = 8$  mm data showing that increasing  $H_f$  at constant impact momentum leads to a decrease in  $H$ . I - VI are the data points corresponding to the flow conditions that are compared in upcoming section.

here  $V_i \approx V_n$  and  $D_i \approx D_n$ . When  $H_f/D_n$  is increased for this  $D_n = 2.7$  mm nozzle, a negligible change in  $H$  is observed. For the larger  $D_n = 8$  mm nozzle (open symbols), Eq. (1.1) accurately predicts the behaviour of  $H$  up to  $\sqrt{V_i V_n D_n} \approx 0.02$  m<sup>2</sup>/s. Beyond this threshold, a transition occurs, and  $H$  scales as  $(V_i V_n)^{1/3} D_n^{2/3}$ , in accordance with the model of Guyot *et al.* (2020) (2/3 power law shown by dashed line). This suggests that beyond a threshold, the buoyancy force becomes dominant over the outgoing momentum flux, leading to a decrease in cloud depth  $H$  compared to what equation (1.1) would predict. Also, Fig. 2 shows the coexistence of two regimes in a narrow range  $\sqrt{V_i V_n D_n} = 0.02 - 0.03$  m<sup>2</sup>/s, wherein the inertia-dominated regime occurs for  $D_n = 2.7$  mm while buoyancy forces become important for the bigger nozzle diameter. This is perhaps a signature of the dependence of the transition threshold on the void fraction at different jet diameters. Finally, in the buoyancy-dominated zone for  $D_n = 8$  mm, some dispersion in the values of  $H$  is observed when  $H_f/D_n$  is varied. As mentioned in the introduction, this dispersion arises from the variations in the net air/water void fraction, as will be discussed in the next subsection.

### 3.2. Local void fraction measurements

The aim of this subsection is to present measurements of the local void fraction  $\phi$  within the bubble cloud and discuss them in relation to the bubble cloud size. We first discuss  $\phi$  measurements along the jet axis, and then radial profiles of  $\phi$  at a given depth within the cloud. Finally, general remarks on the void fraction profiles are presented.

#### 3.2.1. Axial measurements

Figure 3(a) presents air to water volume fraction at the jet axis,  $\phi(r = 0, z)$ , denoted here as  $\phi_0$ . These measurements correspond to the bubble cloud generated by the  $D_n = 2.7$  mm nozzle for two distinct values of jet fall-height to diameter ratio  $H_f/D_n$  while maintaining nearly identical impact momentum. The values of  $\phi_0$  are nearly constant with depth  $z$ , until they sharply decrease at the end of the cloud, as previously reported by van de Donk (1981), McKeogh & Ervine

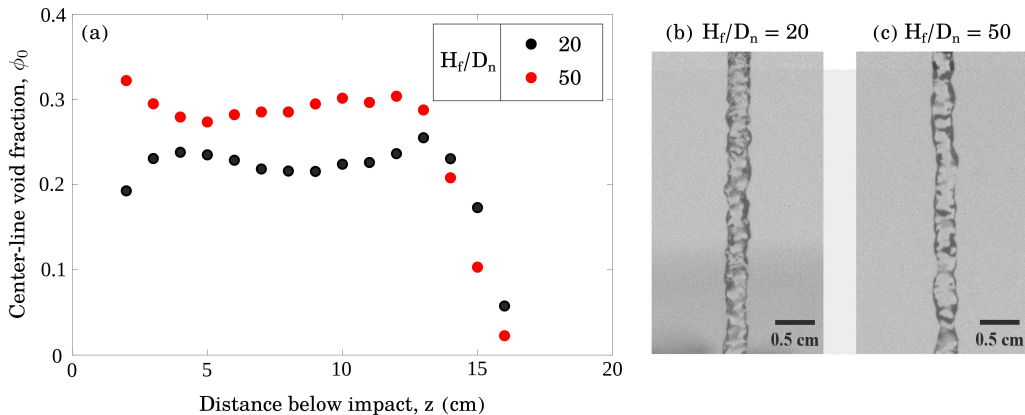


FIGURE 3. (a) Axial evolution of void fraction  $\phi_0(z)$  for two different  $H_f/D_n$  at a fixed jet diameter  $D_n = 2.7$  mm and  $\sqrt{V_i V_n} D_n = 0.016 \pm 0.0002$  m<sup>2</sup>/s. Instantaneous images of the freely-falling jet just before impact are given in (b) and (c).

(1981), Chanson & Manasseh (2003), and Hoque & Aoki (2008). When  $H_f/D_n$  is increased, a similar axial profile is observed, but  $\phi_0$  is increased by almost 26 %.

The jet morphology just before impact is illustrated in Fig. 3(b) and (c) for  $H_f/D_n = 20$  and  $H_f/D_n = 50$ , and it shows a slightly larger amplitude of the jet undulations for the larger  $H_f/D_n$  case. Using the algorithm introduced in Section 2, we measure that the undulations on the jet surface exhibit a roughness of  $\epsilon = 170$   $\mu$ m for Figure 3b and  $\epsilon = 225$   $\mu$ m for Figure 3c. As discussed by McKeogh & Ervine (1981) and Sene (1988), we expect the air entrainment rate and therefore the void fraction to be proportional to the volume enclosed by the corrugations observed on the jet surface. The increase in the size of these undulations is therefore certainly what leads to the increase in void fraction observed in figure 3(a). Supplementary movies 1 and 2 provide additional visualizations of the jets of figure 3(b) and (c) respectively (frame rate of 300 images/s). These two conditions are indicated by labels I and II in Fig. 2. They are both situated in the inertia-dominated regime, where buoyancy effects are still negligible. As a result, the effect of void fraction on  $H$  is negligible, even though  $\phi$  increases.

### 3.2.2. Radial measurements

Radial profiles of the void fraction are measured for three nozzle diameters, and two heights of fall, at a constant impact momentum. The radial profiles are taken at depths larger than  $4D_i$ , in order to ensure they are in the developed region (Ervin & Falvey 1987). Fig. 4(a) shows the bubble cloud generated by a jet of nozzle diameter  $D_n = 2.7$  mm. In comparison, the bubble cloud depth issued from the larger  $D_n = 8$  mm, as shown in Fig. 4(c), is significantly smaller (see also, labels III and IV in Fig. 2). The visualizations of figure 4(a) and (c) are illustrated more extensively in supplementary movies 3 to 6. The void fraction profiles for the 2.7 and 8 mm injectors are shown in Fig. 4(b) and (d), respectively. They are measured for three different depths. Dispersion in  $\phi$  profiles is relatively small in the developed region. These profiles can be well approximated using a Gaussian distribution (solid lines) as previously reported by van de Donk (1981). This finding is similar to the case when an air jet is injected into the pool (Kobus 1968; Freire *et al.* 2002). When our data is compared with fits based on air/bubble diffusivity and air-to-water volume flux ratio, as in Cummings & Chanson (1997), the best fit was found for the air-to-water entrainment ratio of O(10)! This unrealistic value results perhaps from their constant-diffusivity-assumption for advection-diffusion process in the two-phase mixing layer. In our case, and as described by Clanet & Lasheras (1997), the bubbles are convected by the large-scale eddies dominating the evolution of the submerged jet.

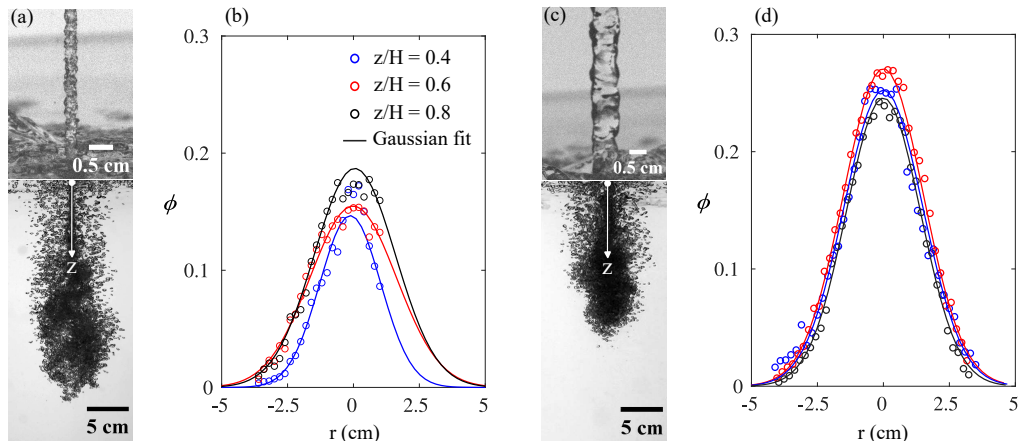


FIGURE 4. (a) and (c) present instantaneous pictures of the falling jet just before impact for  $D_n = 2.7$  and 8 mm, respectively, at constant  $\sqrt{V_n V_i} D_n = 0.028$  m<sup>2</sup>/s and  $H_f/D_n = 20$ . Corresponding bubble clouds are shown as well. (b) and (d) illustrate the radial variation of  $\phi(r, z)$  at three different depths in the bubble cloud, for the 2.7 mm and 8 mm jets, respectively.

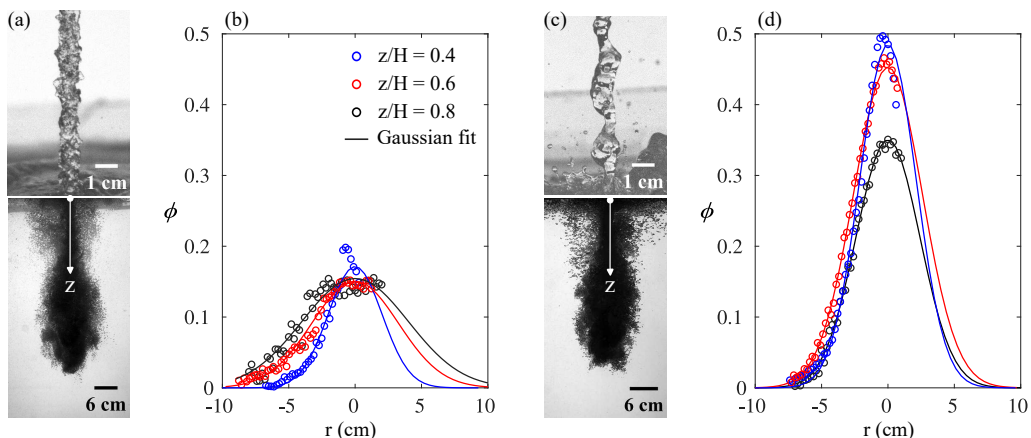


FIGURE 5. Images of  $D_n = 8$  mm jet just before impact for (a)  $H_f/D_n = 20$  and (c) 100, for a constant  $\sqrt{V_n V_i} D_n = 0.075$  m<sup>2</sup>/s. Corresponding bubble clouds are shown as well. (b) and (d) illustrate the radial variation of  $\phi$  at various depths in the bubble clouds for  $H_f/D_n = 20$  and 100 respectively.

Note that the maximum void fraction  $\phi(r = 0, z)$  is significantly smaller for the thinner jet (up to 18 % along the axis, Fig. 4b) when compared with that of the larger jet (up to 27 % in Fig. 4d). The impact of the nozzle diameter on the maximum void fraction has already been evidenced by Chanson *et al.* (2004). The larger void fraction, and hence buoyancy force, is consistent with the observation that the bubble cloud is smaller for the larger diameter. Furthermore, this increase in void fraction is very likely caused by the larger length scales associated with the corrugation and its amplitude occurring on the jet surface when jet diameter  $D_n$  is increased at a constant  $H_f/D_n = 20$  and constant impact momentum (Liu *et al.* 2022; Sene 1988). Measurements of  $\epsilon$  show that the roughness goes from 225  $\mu$ m for Fig. 4b to 445  $\mu$ m for figure 4d. These points are indicated by labels III and IV in Fig. 2. It is clear that III belongs to the momentum-dominated regime, while IV belongs to the buoyancy-dominated regime.

Figure 5 illustrates the influence of a change of the dimensionless jet fall height  $H_f/D_n$ , for a constant impact momentum, and constant diameter  $D_n = 8$  mm. Photographs of the jet before

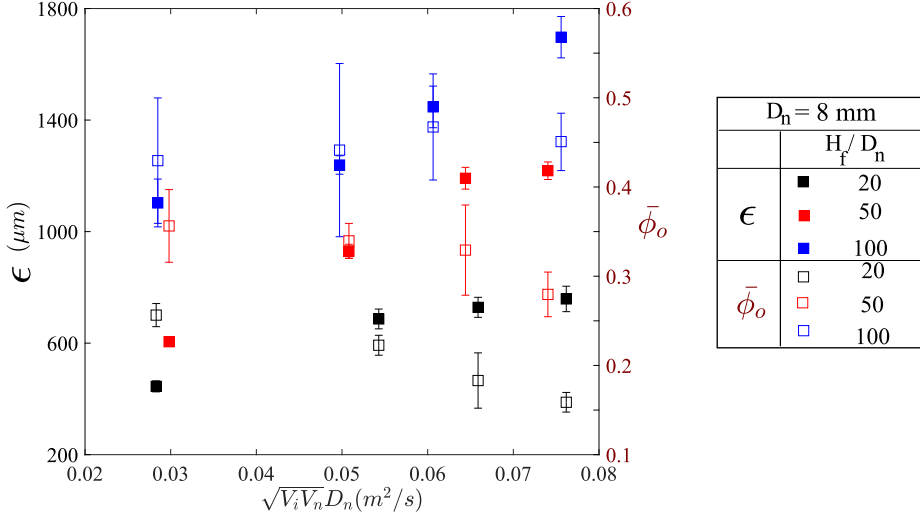


FIGURE 6. Variation of  $\epsilon$  and  $\bar{\phi}_0$  with  $\sqrt{V_i V_n} D_n$  for  $D_n = 8$  mm, where  $\bar{\phi}_0$  is the average over depth of the maximum void fraction measured along the axis. Both  $\epsilon$  and  $\bar{\phi}_0$  increase when  $H_f$  is increased for a constant jet momentum.

impact show that the jet issued at  $H_f/D_n = 100$  (Fig. 5c) is more corrugated than that issued at  $H_f/D_n = 20$  (Fig. 5a), for the same  $\sqrt{V_i V_n} D_n = 0.075$  m<sup>2</sup>/s. This is corroborated by the data of figure 6, which shows the variation of roughness of the jet at impact ( $\epsilon$ ), and the variation of  $\bar{\phi}_0$ , the average over depth of the maximum void fraction measured along the axis, as a function of  $\sqrt{V_i V_n} D_n$  for different  $H_f$ . The data show a strong increase in  $\epsilon$  and  $\bar{\phi}_0$  as  $H_f$  is increased for a constant momentum. The visualizations of figure 5(a) and (c) are illustrated more extensively in supplementary movies 7 to 10. The bubble cloud generated below the surface is smaller for the larger  $H_f/D_n$ . Again, this is likely due to the fact that this jet captures more air within its cavities during free-fall, leading to a higher  $\phi$ . This is confirmed by the radial profiles given in figures 5(b) and (d), which show that  $\phi_0$  for  $H_f/D_n = 100$  is approximately 3.2 times that for  $H_f/D_n = 20$ . Note that these cases are referred to as labels V and VI, respectively, in figure 2. They both correspond to the buoyancy-dominated regime. In addition, the inset displayed in Figure 2 illustrates a zoom view of the change in  $H$  at higher  $\sqrt{V_n V_i} D_n$ , revealing that an increase in  $H_f/D_n$  results in a reduction of  $H$ , with a decrease of approximately 20% observed when  $H_f/D_n$  is raised from 20 to 100. This ascertains that the observed dispersion for the cloud depth in figure 2, and also in previous investigations provided in Guyot *et al.* (2020) for this regime at higher impact momentum and larger diameter, is due to differences in jet fall height.

Finally, general trends of local void fraction profiles are depicted in figure 7 for the case of  $D_n = 8$  mm. Each figure presents data at different vertical locations  $z$  underneath the surface, normalized with respect to the cloud depth  $H$ . In all cases shown here, data fits reasonably well with a Gaussian profile  $\phi = \phi_0(z) e^{-(r^2/\sigma^2(z))}$  whose peak and width do not vary much as  $z/H$  is changed. The first row in figure 7 corresponds to data for the shortest jet fall height to diameter ratio  $H_f/D_n = 20$  at various  $\sqrt{V_i V_n} D_n$ , a measure of the jet impact momentum up to a factor of liquid density. As  $\sqrt{V_i V_n} D_n$  increases the centreline peak void fraction  $\phi_0$  slightly decreases while the width of the best-fitted Gaussian profiles increases. On the other hand, at a given  $\sqrt{V_i V_n} D_n$ , the peak void fraction  $\phi_0$  is almost doubled when the jet's fall height is quintupled. In the next section, these observations on the air/water volume fraction in the biphasic region are further developed to properly capture the effect of buoyancy on the bubble cloud depth.

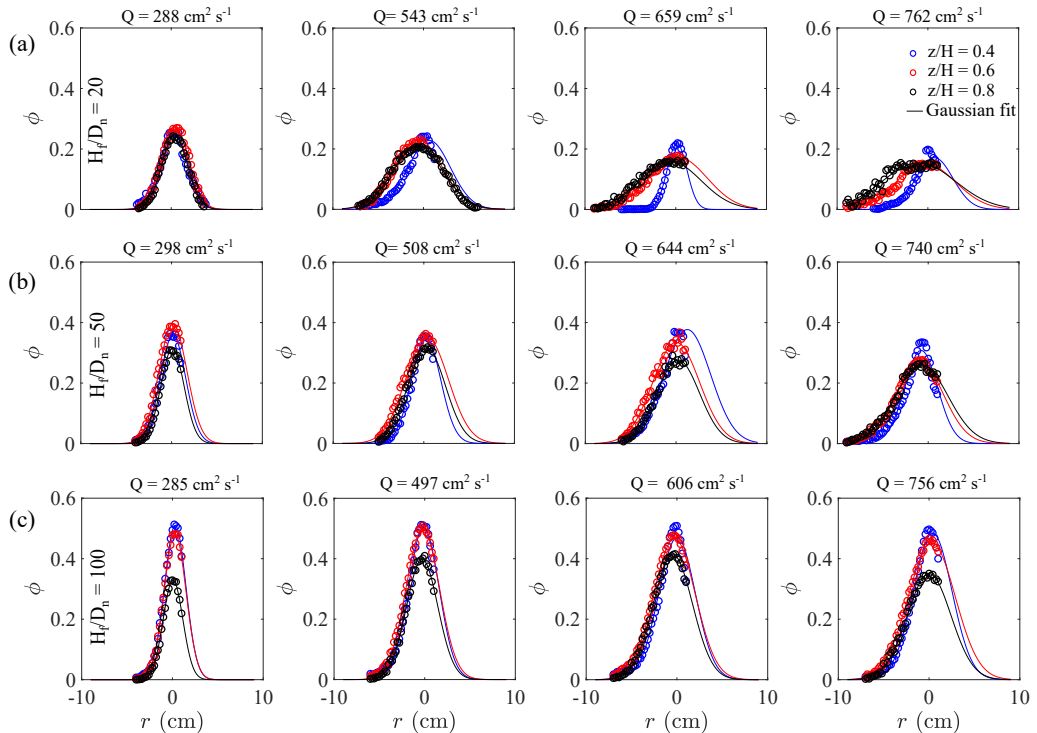


FIGURE 7. Measured profiles of air/water void fraction for the nozzle diameter  $D_n = 8$  mm and different fall-height (a)  $H_f/D_n = 20$ , (b)  $H_f/D_n = 50$ , and (c)  $H_f/D_n = 100$  at various  $Q = \sqrt{V_i V_n} D_n$ . Gaussian fits are represented by continuous lines.

### 3.3. Prediction of bubble cloud depth

Guyot *et al.* (2020) proposed a prediction for the bubble cloud depth  $H$  via Eq. (1.2) by assuming a uniform void fraction within the bubble cloud and a constant cone angle  $\gamma$ , based on single-phase turbulent jets. As mentioned just before, the void fraction in the biphasic jet underneath the free surface can be well-approximated by a Gaussian profile. These profiles are characterised by a maximum void fraction  $\phi_0(z)$  on the axis, and a variance  $\sigma(z)$ . It is then easy to show that the buoyancy force on a slice of bubble cloud of thickness  $dz$  at a depth  $z$  is  $dF_b = \phi_0(z) \rho g \pi \sigma(z)^2 dz$ . We take  $\phi_0(z)$  to be equal to its average value  $\bar{\phi}_0$ , since the peak void fraction  $\phi_0(z)$  exhibits little variation with depth  $z$ , as already shown in figures 3 to 5. It now remains to provide  $\sigma(z)$  in order to integrate this buoyancy force over  $z$ .

Indeed, it is expected that  $\sigma(z)$  increases linearly with depth as the bubble cloud widens up as a cone, as evidenced by visualization and previous observations (Suciu & Smigelschi 1976; McKeogh & Ervine 1981; Clanet & Lasheras 1997; Guyot *et al.* 2020). We propose to measure the angle of this cone based on the experimental void fraction profiles. However, rising bubbles can be detected outside the conical jet region by the optical probe. This may lead to overestimating the width of the void fraction profiles, and hence the resulting buoyancy force on the bubble cloud. This is particularly true for the measurements at shallower depths  $z < 0.5H$ , a problem also encountered by van de Donk (1981). In order to circumvent this difficulty, the conical jet hypothesis is maintained in accordance with previous authors so that  $\sigma(z) = D_i/2 + z \tan \gamma_0$ , where the cone angle  $\gamma_0$  is computed as  $\tan \gamma_0 = (\sigma(\bar{z}) - D_i/2) / \bar{z}$  at a chosen reference depth  $\bar{z} = 0.8H$ . The latter depth was chosen to avoid both rising bubbles and the steep decrease in bubble void fraction in the neighbourhood of the cloud's tail at  $z = H$ .

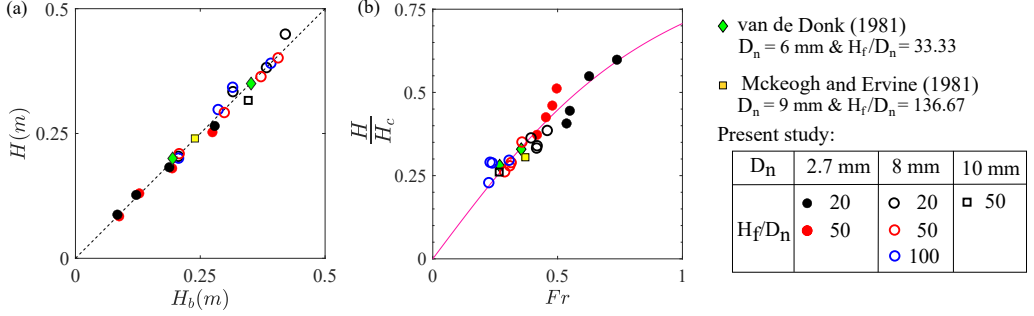


FIGURE 8. (a) Comparison of experimental depth  $H$  with those predicted by the model  $H_b$  and (b) Normalized depth  $H/H_c$  at various  $Fr$  for injectors from current and past studies whose void fraction is known. Eq. (3.2) is represented by the continuous line.

Thereby, the net buoyancy force  $F_b$  on the bubble cloud of depth  $H_b$  can then be expressed as

$$F_b = \bar{\phi}_0 \rho g \pi \left( \frac{1}{3} H_b^3 \tan^2 \gamma_0 + \frac{D_i}{2} H_b^2 \tan \gamma_0 + \frac{D_i^2}{4} H_b \right), \quad (3.1)$$

which is identical to the volume term in Eq. (1.2), if  $\bar{\phi} = \bar{\phi}_0$  and  $\gamma = \gamma_0$ . The above expression indicates that the buoyancy force on a conical biphasic jet exhibiting a Gaussian void fraction profile can be interpreted as the buoyancy force exerted on an equivalent biphasic jet with a constant void fraction  $\bar{\phi}$  equal to the *maximum* void fraction  $\bar{\phi}_0$  of the Gaussian profile, and with a width defined by the variance of the Gaussian profile at some reference depth, here chosen at  $z = 0.8H$ . This buoyancy force  $F_b$  can now be injected into the momentum balance (equation 1.2) in order to solve for  $H_b$ . The value of  $\bar{\phi}$  in the outgoing momentum term can be taken equal to  $\bar{\phi}_0$  for the sake of simplicity.

Experimental depths  $H$  from the present study and predictions  $H_b$  are compared in Fig. 8(a) for the different nozzle sizes and jet fall heights. A good agreement is found between the model and measurements for both the inertia-controlled bubble clouds ( $D_n = 2.7$  mm) and the buoyancy-controlled ( $D_n = 8$  mm and 10 mm) ones. A measurement for nozzle diameter  $D_n = 10$  mm (same length-to-diameter ratio of 50),  $V_n = 5.5$  m/s and  $H_f/D_n = 50$  has been included in the data of this figure. For comparison, two previous investigations, namely, those conducted by van de Donk (1981) and McKeogh & Ervine (1981) are presented in Fig. 8(a) as well. They provided both  $H$  measurements and radial profiles of  $\phi$  for jets with diameters of  $D_n = 6$  and 9 mm. The calculated  $H_b$  values based on their measurements show a very good consistency with the model.

In what follows, the question of the role of void fraction in the transition from the inertia-dominated to the buoyancy-dominated regime is discussed. This transition is expected to be dominated by the ratio of the outgoing momentum to buoyancy force, respectively second and third terms in Eq. (1.2). The square root of the ratio of these terms defines a dimensionless grouping similar to a Froude number, referred to as  $Fr = \sqrt{3(1 - \bar{\phi}_0) / \bar{\phi}_0} U_i / \sqrt{gH_b}$ . In fact, when the nozzle diameter is small compared to the cloud width  $2H_b \tan \gamma_0$ , the cubic polynomial for  $H_b$  in Eq. (1.2) can be rewritten in terms of  $Fr$  as

$$\frac{H_b}{H_c} = \frac{Fr}{\sqrt{1 + Fr^2}} + O\left(\frac{D_i}{2H_b \tan \gamma_0} Fr^2\right), \quad (3.2)$$

where  $H_c$  is the cloud depth when the buoyancy force is absent, as given by Eq. (1.1). When  $Fr$  is large, we expect the cloud to be in the inertia-dominated regime, and hence  $H_b$  to be close to  $H_c$ , the simple prediction by Clanet & Lasheras (1997). When on the contrary  $Fr$  is small,  $H$  is expected to be controlled by buoyancy, and hence to be significantly smaller than  $H_c$ . Figure

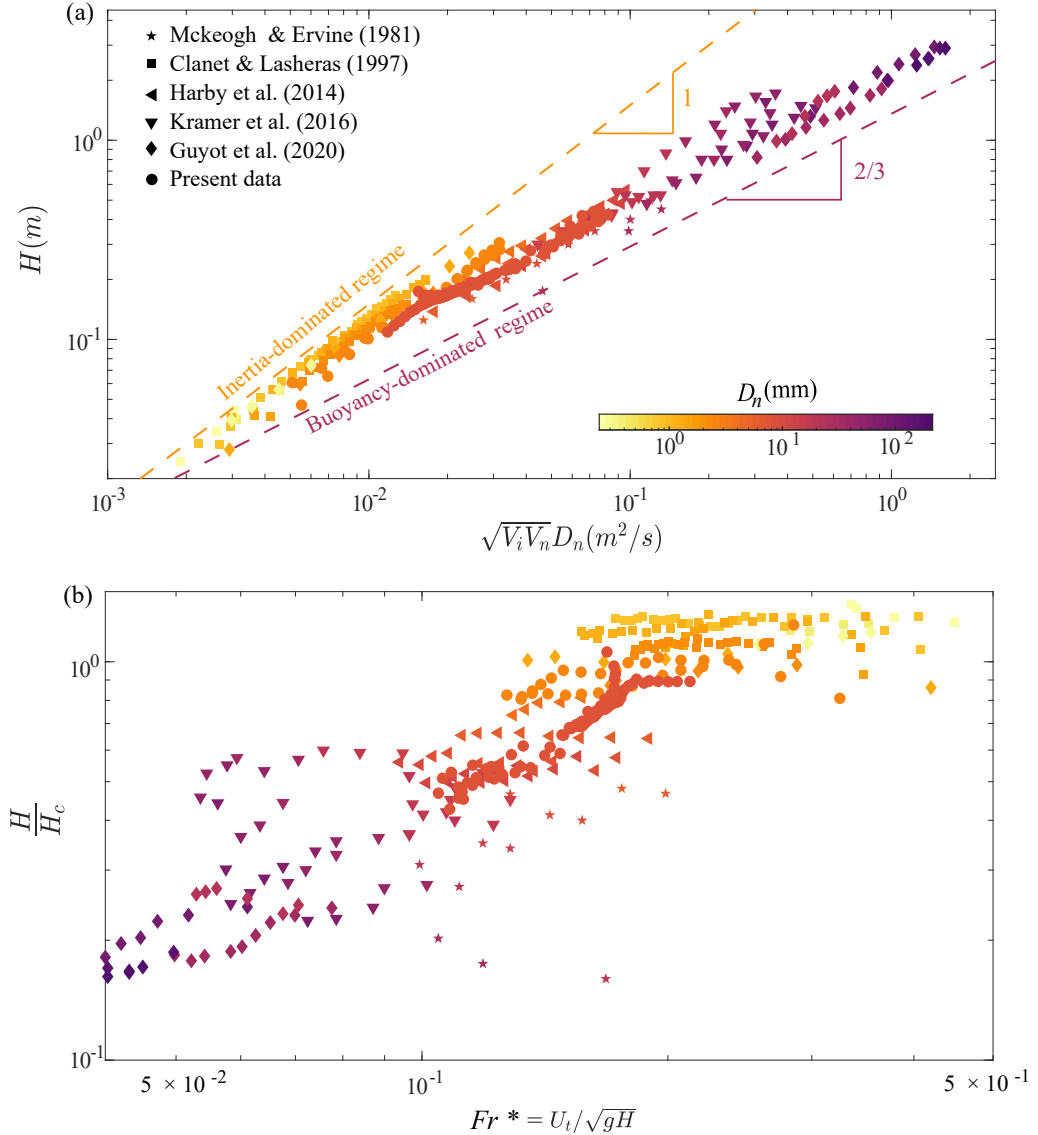


FIGURE 9. (a) Bubble cloud depth ( $H$ ) data from previous investigations are presented here as a function of  $\sqrt{V_i V_n} D_n$ , a measure of the impact momentum, to illustrate the two distinct dynamical regimes identified in our study over a wide range of scales. (b) When void fraction is not known,  $Fr^*$  can still sort past experiments into inertia or buoyancy-dominated regimes, even though more dispersion is observed.

8(b) illustrates the variation of  $H/H_c$  with  $Fr$  for data from Fig. 8(a). Indeed, all experimental data points fall on a single curve given by Eq. (3.2), for which  $H/H_c$  falls steeply when  $Fr$  is decreased. For a constant velocity, using larger nozzles will lead to bigger bubble clouds, and so larger  $H$  and smaller  $Fr$ , thereby favouring the buoyancy-dominated regime. Note also that the influence of jet velocity is counter-intuitive here since a larger jet velocity for a given nozzle diameter will generate a larger  $H$ , and therefore also favour the buoyancy-dominated regime, instead of the inertial regime. This is because the relevant velocity scale in  $Fr$  is the terminal bubble velocity  $U_t$ , which is a constant, and not the jet impact velocity. Note that expression (3.2) is obtained from Eq. (1.2) by assuming  $\bar{\phi} = \bar{\phi}_0$  and  $\gamma = \gamma_0$ . This choice simplifies the expression

of the Froude number, but obviously underestimates the jet angle and mean void fraction in the inertial contribution. This is partly the reason why  $H/H_c$  does not reach the limit  $H/H_c = 1$  in figure 8(b), even for data points which corresponded to the inertia-dominated regime in Fig. 2. Furthermore, previous authors have proposed to add a hemispherical dome to the truncated cone modelling the bubble cloud, as in figure 1 (Clanet & Lasheras 1997; Guyot *et al.* 2020). This small correction would introduce a factor  $1 + \tan \gamma_0$  (of the order of 10 %) to both the modelled heights  $H_c$  and  $H_b$ , but is not considered in the present data for the sake of simplicity.

For most studies for which bubble cloud depths data are available, the void fraction has not been measured concomitantly. We plot on Fig. 9(a)  $H$  as a function  $\sqrt{V_i V_n} D_n$ , square-root of the impact momentum over liquid density  $\rho$ , for five past studies covering a wide range of scales, plus the present data. The scaling laws observed in figure 2, for the inertia-dominated and buoyancy-dominated regimes, can be observed in the limit of low momentum and large momentum respectively. The void fraction is not known for these past works, but we can still estimate the bubble cloud Froude number as  $Fr^* = U_i / \sqrt{gH}$ . Figure 9(b) shows that when  $H/H_c$  is plotted as a function of  $Fr^*$  for several past studies, the cloud sizes are clearly sorted in two regimes: (i) One for larger  $Fr^* > 0.2$  for which  $H/H_c$  is close to one, and for which there is little dispersion, and (ii) A second regime for  $Fr^* < 0.2$  where  $H/H_c$  varies between 0.15 and 0.5, and for which a significant dispersion is obtained. This dispersion is very likely due to the role of the void fraction, which has been omitted in  $Fr^*$ . These observations further ascertain that  $Fr$  is a good parameter to monitor the transition between the inertia-dominated and the buoyancy-dominated regime.

### 3.4. Equivalent bubble cloud void fraction $\phi_b$

Whereas Guyot *et al.* (2020) took a uniform void fraction within the cloud to express the momentum balance,  $\phi$  profiles were observed here to follow a Gaussian distribution in the radial direction. In this section, an *equivalent* constant void fraction  $\phi_b$  is proposed in order to provide a bulk quantity for a bubble cloud and to discuss its variations with the jet fall height and impact momentum. At first, for a fixed depth  $z$ , the edge of this constant-void-fraction-cone of bubble cloud is defined by admitting that its radius  $R_b(z)$ , beyond which the void fraction becomes zero, is the radius at which 80% of the surface-integrated void fraction is attained based on a Gaussian profile  $\phi = \bar{\phi}_0(z) e^{-r^2/\sigma(z)^2}$ . This simply gives the relation  $R_b(z) = \sigma(z) \sqrt{\log 5} \approx 1.27\sigma$ . Thereafter, in order to avoid over-estimation of the bubble cloud volume due to rising bubbles, the truncated cone angle  $\gamma_b$  for this constant-void-fraction cloud is taken as  $\tan \gamma_b = (\tilde{R}_b - D_i/2)/\tilde{z}$  where  $\tilde{R}_b \approx 1.27\sigma(\tilde{z})$  is this cloud's radius at the reference depth  $\tilde{z} = 0.8H$ . As already mentioned in section 3.3, the influence of rising bubbles is minimal at the reference depth  $\tilde{z} = 0.8H$ , measured close to the bottom of the cloud while the *peak* void fraction  $\phi_0$  is still comparable to those obtained in the bulk. Finally, the *equivalent* void fraction  $\phi_b$  is then computed such that the net buoyancy force is the same on both the uniform-void-fraction cloud and the Gaussian-void-fraction cloud.

Figures 10(b) and (d) depict the evolution of this *equivalent* void fraction  $\phi_b$  as a function of  $H_f/D_n$ , for different values of impact momentum (represented by the colour) for the two injectors. Experimental results show that  $\phi_b$  increases steeply for both injectors as  $H_f/D_n$  increases, as already illustrated in figure 5 for a particular case. As mentioned in subsection 3.2.2, this is likely due to the jet's capacity to entrain more air once perturbations have grown larger on its surface for higher fall height  $H_f$  (Sene 1988). These plots also show that  $\phi_b$  decreases for a constant  $H_f/D_n$  as the impact momentum is increased, in particular for low  $H_f/D_n$ .

Figure 10(c) and (e) illustrate the variations of the cone angle  $\gamma_b$  of the *equivalent* constant- $\phi$  jet with regards to  $H_f/D_n$ , for different  $\sqrt{V_i V_n} D_n$ . Results for both nozzles show that  $\gamma_b$  decreases with  $H_f/D_n$  for a constant impact momentum. This change in the bubble cloud shape may be related to the strong increase in the amplitude of surface perturbations at larger  $H_f$  and to the

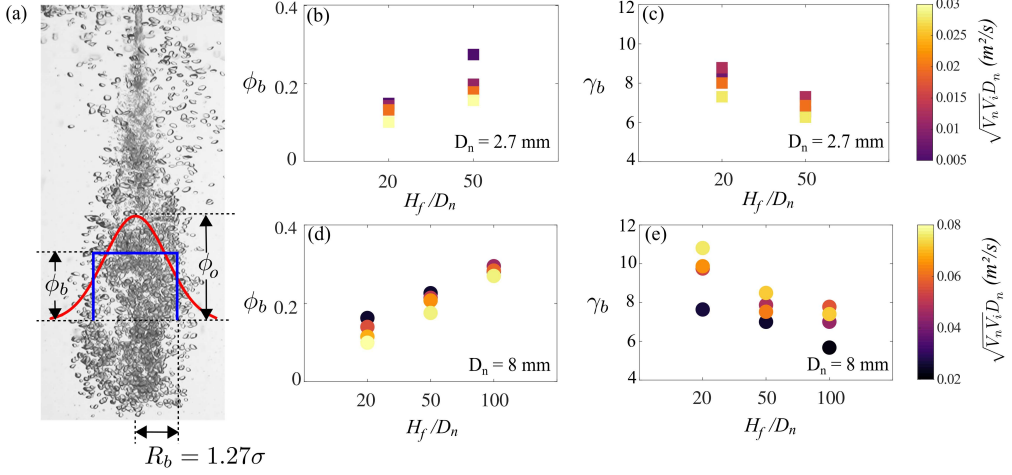


FIGURE 10. (a) Definition of  $\Phi_b$  and  $R_b$ . (b) Variation of  $\Phi_b$  and  $\gamma_b$  with  $H_f/D_n$  for the two injector sizes at various impact momentum. Two color bars are provided for the two ranges of  $\sqrt{V_i V_n} D_n$ , corresponding to both  $D_n$  values.

larger void fractions observed for these conditions ( $\phi_0$  up to 50% for  $H_f/D_n = 100$ , compared to 20% for  $H_f/D_n = 20$ ). The simple assumptions made regarding the shape of the bubble cloud, which are valid at moderate void fractions, probably do not hold anymore in such conditions.

#### 4. Conclusion

Experiments on circular plunging jets have been carried out to characterize the two regimes for bubble cloud formation, namely the inertia-dominated and the buoyancy-dominated regimes. Void fraction profiles were measured in the developed region of the cloud with novel optical probes for nozzle diameter,  $D_n = 2.7, 8$  and  $10$  mm. They can be well approximated by Gaussian distributions. When these measurements are incorporated into the momentum balance model, taking into account only the buoyancy force, it predicts the experiments very well for both current and past studies. Even though the void fraction measurements have only been carried out for nozzle sizes smaller than  $1$  cm and bubble cloud sizes smaller than  $50$  cm, it is expected that this result still holds at larger scales, as already proposed by Guyot *et al.* (2020). This will have to be verified with void fraction measurements in such metric scale systems in future works.

The threshold between the inertia and buoyancy regimes is shown to be dependent on a *characteristic* Froude number  $Fr$  built with the terminal bubble velocity  $U_t$ , the cloud depth  $H$ , and the void fraction within the bubble cloud. For large values of this number,  $H$  can be estimated with the simple model of Clanet & Lasheras (1997), while for low values of  $Fr$ , it is buoyancy that controls the bubble cloud size. The fact that a single equation can predict bubble cloud size independent of scale and of the wide zoology of jet dynamics provided the void fraction is known is the major result of this work.

A constant *equivalent* void fraction  $\phi_b$  is also introduced based on the integration of the Gaussian void fraction profiles. The variations of  $\phi_b$  and of the corresponding jet cone angle  $\gamma_b$  with the impact momentum and the jet fall-height to diameter ratio  $H_f/D_n$  are discussed. This void fraction  $\phi_b$  is expected to be a function of jet diameter, the height of fall, and velocity (Wang *et al.* 2018). Data show that an increase in the height of fall  $H_f$  leads to a significant increase in the void fraction within the cloud, which in turn leads to a decrease in the bubble cloud size. The modelling of  $\phi_b$  as a function of jet dynamics, which is necessary for practical

purposes if one wishes to predict  $H$  solely as a function of input parameters, is the question future works will have to address.

**Acknowledgements.** We acknowledge the technical support of G. Geniquet, S. Martinez and A. Buridon on the experimental set-up. We also thank A2 Photonic Sensors for the support with the optical probes. This research was funded by the French Agence Nationale de la Recherche ANR under grant no. JETPLUME ANR-21-CE05-0029.

**Funding.** - This research was funded by the French Agence Nationale de la Recherche ANR under grant no. JETPLUME ANR-21-CE05-0029.

**Declaration of interest.** The authors report no conflict of interest.

**Author ORCIDs.** Narendra Dev, <https://orcid.org/0009-0007-4626-3585>; J. John Soundar Jerome, <https://orcid.org/0000-0003-2148-9434>; H. Scolan, <https://orcid.org/0000-0003-2739-2297>; J.-P. Matas, <https://orcid.org/0000-0003-0708-1619>;

## REFERENCES

- BERTOLA, N., WANG, H. & CHANSON, H. 2018 A physical study of air–water flow in planar plunging water jet with large inflow distance. *International Journal of Multiphase Flow* **100**, 155–171.
- BIŃ, ANDRZEJ K 1993 Gas entrainment by plunging liquid jets. *Chemical Engineering Science* **48** (21), 3585–3630.
- BONETTO, F, DREW, D & LAHEY JR, RT 1994 The analysis of a plunging liquid jet – the air entrainment process. *Chemical Engineering Communications* **130** (1), 11–29.
- BONETTO, F. & LAHEY, R. T. 1993 An experimental study on air carryunder due to a plunging liquid jet. *International Journal of Multiphase Flow* **19** (2), 281–294.
- BRATTBERG, T. & CHANSON, H. 1998 Air entrapment and air bubble dispersion at two-dimensional plunging water jets. *Chemical engineering science* **53** (24), 4113–4127.
- CHANSON, H. 2002 *Hydraulics of stepped chutes and spillways*. CRC Press.
- CHANSON, H., AOKI, S. & HOQUE, A. 2004 Physical modelling and similitude of air bubble entrainment at vertical circular plunging jets. *Chemical engineering science* **59** (4), 747–758.
- CHANSON, H. & MANASSEH, R. 2003 Air entrainment processes in a circular plunging jet: Void-fraction and acoustic measurements. *J. Fluids Eng.* **125** (5), 910–921.
- CHIRICHELLA, D., GOMEZ LEDESMA, R., KIGER, K. T. & DUNCAN, J. H. 2002 Incipient air entrainment in a translating axisymmetric plunging laminar jet. *Physics of Fluids* **14** (2), 781–790.
- CLANET, C. & LASHERAS, J. C. 1997 Depth of penetration of bubbles entrained by a plunging water jet. *Physics of Fluids* **9** (7), 1864–1866.
- CUMMINGS, P.D. & CHANSON, H. 1999 An experimental study of individual air bubble entrainment at a planar plunging jet. *Chemical Engineering Research and Design* **77** (2), 159–164.
- CUMMINGS, P. D. & CHANSON, H. 1997 Air Entrainment in the Developing Flow Region of Plunging Jets—Part 1: Theoretical Development. *Journal of Fluids Engineering* **119** (3), 597–602.
- VAN DE DONK, J. A. C. 1981 Water aeration with plunging jets. PhD thesis, Delf University of Technology Delf, The Netherland.
- EL HAMMOUMI, M., ACHARD, J.-L. & DAVOUST, L. 2002 Measurements of air entrainment by vertical plunging liquid jets. *Experiments in fluids* **32**, 624–638.
- ERVINE, D.A. & FALVEY, H.T. 1987 Behaviour of turbulent water jets in the atmosphere and in plunge pools. *Proceedings of the Institution of Civil engineers* **83** (1), 295–314.
- FREIRE, A. P. S., MIRANDA, D. D. E., LUZ, L. M. S. & FRANÇA, G. F. M. 2002 Bubble plumes and the coanda effect. *International journal of multiphase flow* **28** (8), 1293–1310.
- GUYOT, GREÉGORI 2019 Contribution à la caractérisation des processus d’entraînement d’air dans les circuits d’aménagements hydro-électriques. PhD thesis, Université Grenoble Alpes, France.
- GUYOT, G., CARTELLIER, A. & MATAS, J.-P. 2019 Depth of penetration of bubbles entrained by an oscillated plunging water jet. *Chemical Engineering Science: X* **2**, 100017.
- GUYOT, G., CARTELLIER, A. & MATAS, J.-P. 2020 Penetration depth of a plunging jet: from microjets to cascades. *Physical Review Letters* **124** (19), 194503.

- HARBY, K., CHIVA, S. & MUÑOZ-COBO, J.L. 2014 An experimental study on bubble entrainment and flow characteristics of vertical plunging water jets. *Experimental Thermal and Fluid Science* **57**, 207–220.
- HOQUE, A. & AOKI, S. 2008 Air entrainment and associated energy dissipation in steady and unsteady plunging jets at free surface. *Applied Ocean Research* **30** (1), 37–45.
- HORN, G. & THRING, M.W. 1956 Angle of spread of free jets. *Nature* **178** (4526), 205–206.
- KAPUR, J.N., SAHOO, P.K. & WONG, A.K.C. 1985 A new method for gray-level picture thresholding using the entropy of the histogram. *Computer Vision, Graphics, and Image Processing* **29** (3), 273–285.
- KIGER, K. T. & DUNCAN, J. H. 2012 Air-entrainment mechanisms in plunging jets and breaking waves. *Annual Review of Fluid Mechanics* **44**, 563–596.
- KIRILLOV, A., MINTUN, E., RAVI, N., MAO, H., ROLLAND, C., GUSTAFSON, L., XIAO, T., WHITEHEAD, S., BERG, A. C. Lo, W.-Y. & OTHERS 2023 Segment anything. *arXiv preprint arXiv:2304.02643*.
- KOBUS, H. E. 1968 Analysis of the flow induced by air-bubble systems. In *Coastal Engineering 1968*, pp. 1016–1031.
- KRAMER, M., WIEPRECHT, S. & TERHEIDEN, K. 2016 Penetration depth of plunging liquid jets—a data driven modelling approach. *Experimental Thermal and Fluid Science* **76**, 109–117.
- LIN, T. J. & DONNELLY, H. G. 1966 Gas bubble entrainment by plunging laminar liquid jets. *AIChE Journal* **12** (3), 563–571.
- LIU, C., GAO, R. & HU, C. 2022 A consistent mass–momentum flux computation method for the simulation of plunging jet. *Physics of Fluids* **34** (3), 032114.
- LIU, S., ZENG, Z., REN, T., LI, F., ZHANG, H., YANG, J., LI, C., YANG, J., SU, H., ZHU, J. & OTHERS 2023 Grounding dino: Marrying dino with grounded pre-training for open-set object detection. *arXiv preprint arXiv:2303.05499*.
- LORENCEAU, ÉLISE, QUÉRÉ, DAVID & EGGERS, JENS 2004 Air entrainment by a viscous jet plunging into a bath. *Physical review letters* **93** (25), 254501.
- L'VOV, VICTOR S, POMYALOV, ANNA, PROCACCIA, ITAMAR & GOVINDARAJAN, RAMA 2008 Random vortex-street model for a self-similar plane turbulent jet. *Physical review letters* **101** (9), 094503.
- MA, J, OBERAI, AA, DREW, DA, LAHEY JR, RT & MORAGA, FJ 2010 A quantitative sub-grid air entrainment model for bubbly flows—plunging jets. *Computers & Fluids* **39** (1), 77–86.
- MAXWORTHY, T, GNANN, C, KÜRTEEN, M & DURST, F 1996 Experiments on the rise of air bubbles in clean viscous liquids. *Journal of fluid mechanics* **321**, 421–441.
- MCKEOGH, E.J. & ERVINE, D.A. 1981 Air entrainment rate and diffusion pattern of plunging liquid jets. *Chemical Engineering Science* **36** (7), 1161–1172.
- MIWA, S., MORIBE, T., TSUTSUMI, K. & HIBIKI, T. 2018 Experimental investigation of air entrainment by vertical plunging liquid jet. *Chemical Engineering Science* **181**, 251–263.
- QU, X., GOHARZADEH, A., KHEZZAR, L. & MOLKI, A. 2013 Experimental characterization of air-entrainment in a plunging jet. *Experimental Thermal and Fluid Science* **44**, 51–61.
- ROY, A. K., MAITI, B. & DAS, P. K. 2013 Visualisation of air entrainment by a plunging jet. *Procedia Engineering* **56**, 468–473.
- VAN DE SANDE, E & SMITH, JOHN M 1973 Surface entrainment of air by high velocity water jets. *Chemical Engineering Science* **28** (5), 1161–1168.
- VAN DE SANDE, E & SMITH, JOHN M 1976 Jet break-up and air entrainment by low velocity turbulent water jets. *Chemical Engineering Science* **31** (3), 219–224.
- SCHINDELIN, JOHANNES, ARGANDA-CARRERAS, IGNACIO, FRISE, ERWIN, KAYNIG, VERENA, LONGAIR, MARK, PIETZSCH, TOBIAS, PREIBISCH, STEPHAN, RUEDEN, CURTIS, SAALFELD, STEPHAN, SCHMID, BENJAMIN & OTHERS 2012 Fiji: an open-source platform for biological-image analysis. *Nature methods* **9** (7), 676–682.
- SENE, K.J. 1988 Air entrainment by plunging jets. *Chemical Engineering Science* **43** (10), 2615–2623.
- SPEIRS, NATHAN B, PAN, ZHAO, BELDEN, JESSE & TRUSCOTT, TADD T 2018 The water entry of multi-droplet streams and jets. *Journal of Fluid Mechanics* **844**, 1084–1111.
- SUCIU, G.D. & SMIGELSKI, O. 1976 Gas absorption by turbulent liquid plunging jets. *Chemical Engineering Sciences – Shorter Communications* **32**, 889–896.
- TSAI, WEN-HSIANG 1985 Moment-preserving thresholding: A new approach. *Computer Vision, Graphics, and Image Processing* **29** (3), 377–393.
- WANG, H., SLAMET, N. S., ZHANG, G. & CHANSON, H. 2018 Intrusive measurements of air-water flow properties in highly turbulent supported plunging jets and effects of inflow jet conditions. *Chemical Engineering Science* **177**, 245–260.

ZHU, Y., OĞUZ, H. N. & PROSPERETTI, A. 2000 On the mechanism of air entrainment by liquid jets at a free surface. *Journal of Fluid Mechanics* **404**, 151–177.